ACS APPLIED MATERIALS & INTERFACES

Research Article

www.acsami.org

Nanostructure of Fully Injectable Hydrazone–Thiosuccinimide Interpenetrating Polymer Network Hydrogels Assessed by Small-Angle Neutron Scattering and dSTORM Single-Molecule Fluorescence Microscopy

Trevor Gilbert,[†] Richard J. Alsop,[‡] Mouhanad Babi,[§] José Moran-Mirabal,[§] Maikel C. Rheinstädter,[‡] and Todd Hoare*[,†]

[†]Department of Chemical Engineering, McMaster University, 1280 Main St. W, Hamilton, Ontario L8S 4L7, Canada

[‡]Department of Physics and Astronomy and [§]Department of Chemistry and Chemical Biology, McMaster University, 1280 Main St. W, Hamilton, Ontario L8S 4M1, Canada

Supporting Information

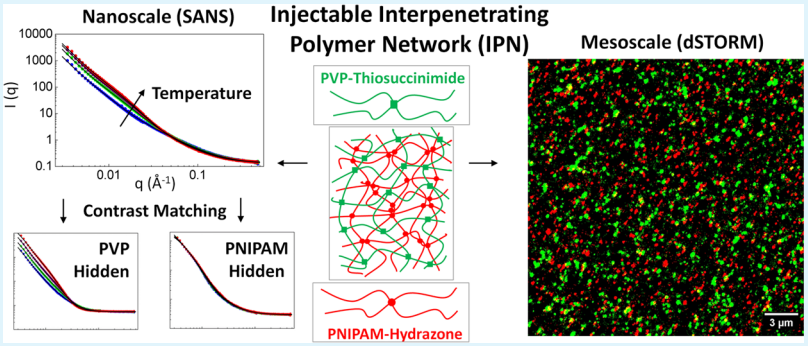

ABSTRACT: Herein, we comprehensively investigate the internal morphology of fully injectable interpenetrating networks (IPNs) prepared via coextrusion of functionalized precursor polymer solutions based on thermoresponsive poly(*N*-isopropylacrylamide) (PNIPAM) and nonthermoresponsive poly(vinyl pyrrolidone) (PVP) by reactive mixing using kinetically orthogonal hydrazone and thiosuccinimide cross-linking mechanisms. Small-angle neutron scattering, probing both the full IPN as well as the individual constituent networks of the IPN using index-matching, suggests a partially mixed internal structure characterized by PNIPAM-rich domains entrapped in a clustered PVP-rich phase. This interpretation is supported by super-resolution fluorescence microscopy (direct stochastic optical reconstruction microscopy) measurements on the same gels on a different length scale, which show both the overall phase segregation typical of an IPN as well as moderate mixing of PNIPAM into the PVP-rich phase. Such a morphology is consistent with the kinetics of both gelation and phase separation in this in situ gelling system, in which gelation effectively traps a fraction of the PNIPAM in the PVP phase prior to full phase separation; by contrast, such interphase mixing is not observed in semi-IPN control hydrogels. This knowledge has significant potential for the design of an injectable hydrogel with internal morphologies optimized for particular biomedical applications.

KEYWORDS: *interpenetrating network (IPN) hydrogel, fully injectable, internal morphology*

INTRODUCTION

Interpenetrating network (IPN) hydrogels are distinguished by the interlocking of two independently cross-linked but chemically noninteracting networks that swell in water.[1] Much of the interest in hydrogel IPNs has stemmed from the proven degree of mechanical enhancement[2] that is achievable relative to the constituent single networks as a result of the physical entanglements that form between the networks. Although such enhancements are particularly notable with double-network IPNs consisting of one weakly cross-linked and one highly cross-linked component,[3,4] such mechanical enhancements are more broadly used to increase the stiffness of various hydrogels for potential use in load-bearing applications (e.g., stiffer tissue scaffolds for cartilage[5] or bone[6]). However, the internal structure of IPNs can also be leveraged effectively in targeted applications. The formation of distinctive network micro- and nanostructures in IPNs and semi-IPNs can be used to regulate the pore size/morphology (facilitating control over diffusion properties for separation applications[7] or drug delivery[8]) as well as to facilitate the creation of a network of segregated domains enriched with one or the other component polymer network (facilitating, e.g.,

Received: August 9, 2017
Accepted: November 13, 2017
Published: November 13, 2017

DOI: 10.1021/acsami.7b11637
ACS Appl. Mater. Interfaces 2017, 9, 42179–42191

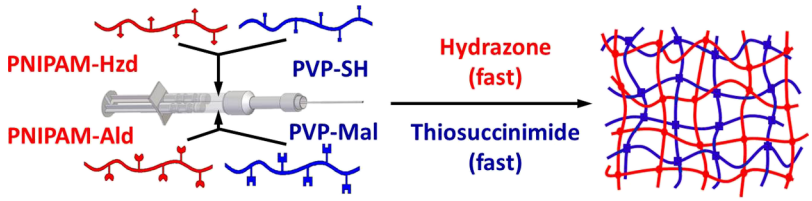

Figure 1. Schematic of chemistry and gelation strategy used for injectable IPN formation.

enhanced uptake and subsequent control over release of drugs with specific properties[9]).

The morphologies formed in hydrogel IPNs are dependent on the kinetics of gel network formation in the two constituent networks[10] as well as on the propensity for phase separation between the two networks under the environmental conditions in which they are prepared.[11] The former is particularly important in regulating the morphology development in simultaneous IPNs in which both networks form via orthogonal chemistries; specifically, faster and more closely matched network formation rates between the two constituents generally favor more homogeneous IPNs.[10] Furthermore, for systems in which phase separation is thermodynamically favored but the rate of network formation exceeds that of diffusion-based mass transfer, gelation can "lock in" otherwise unfavorable morphologies[4] and significantly influence the ultimate morphology achieved in the IPN system.

A thorough characterization of these structural features is a necessity for the rational design of network architecture for particular applications.[1,12] In particular, the capacity for partial domain segregation is of particular interest for predicting the performance of IPNs as cell scaffolds and/or drug-delivery materials, as domain segregation is expected to significantly alter the capacity for drug uptake as well as both the partitioning and diffusion-based barriers to the subsequent release of that drug. Several methods have been applied to study the nature of domain formation in IPN hydrogels, including differential scanning calorimetry,[13,14] electron microscopy,[15] laser scanning confocal microscopy,[16] and small-angle neutron scattering (SANS).[17] However, among these methods, only SANS is capable of providing nanometer-scale information about the nature of the network structure in the swollen state, which is the key piece of information required to effectively engineer hydrogel IPNs with specific morphological features. The technique of contrast-matching SANS, in which the deuterium/hydrogen ratio of the solvent is adjusted to match the neutron-scattering length density of a material being probed, is particularly useful for individually probing the nanostructures of each IPN in the presence of the other network; this technique has been used previously to characterize the response of brittle−ductile double-network IPN hydrogels to tensile strain.[18,19] By preparing samples with one network made from the deuterated analogue monomer in aqueous solvents with different hydrogen/deuterium ratios that separately match the scattering length density of each of the component phases, scattering contributions from the network that is matched to the solvent are suppressed (i.e., that network is "invisible"), and the network structure of the other interpenetrating phase can be independently elucidated. This technique has also previously been applied to investigate the morphology of poly(*N*-isopropylacrylamide) (PNIPAM)−clay composites,[20] magnetic nanoparticle-loaded hydrogels,[21] and poly(ethylene glycol)/poly(acrylic acid) IPNs.[22]

The recent development of super-resolution fluorescence techniques, such as direct stochastic optical reconstruction microscopy (dSTORM), has provided an additional possible avenue for the exploration of nano- and microstructures of gel IPN systems. The technique is based on reversibly switching fluorophores between active and inactive states,[23,24] with a sparse subset of all fluorophores active at any given time. Fitting the two-dimensional point-spread function around single fluorophores can allow localization of the emitter to less than the diffraction limit associated with the resolution of conventional microscopy.[25] By collecting image stacks covering long acquisition times, the randomly sampled super-resolution localizations collected in each frame can be added to reconstruct the locations of the entire population of fluorophores. Although this approach has been used extensively for biological applications, such as live cell imaging,[26,27] tracking assembly of the viral envelope in HIV,[28] and tracking actin and myosin dynamics in the skeletal muscle,[29] and for materials applications, such as assessing chain distributions within the core−shell[30] or innately inhomogeneous[31] PNIPAM microgels, multichannel dSTORM imaging has not to our knowledge previously been applied to study phase segregation and internal morphology in IPNs or other multicomponent bulk hydrogels.

Recently, we reported a fully injectable simultaneous IPN that forms by kinetically orthogonal mixing of two pairs of functionalized prepolymers: hydrazide-functionalized PNIPAM and thiol-functionalized poly(vinyl pyrrolidone) (PVP) mixed through a double-barreled syringe with aldehyde-functionalized PNIPAM and maleimide-functionalized PVP[30] (Figure 1). Such a protocol results in a hydrazone-cross-linked thermosensitive network interpenetrated with a thiosuccinimide-cross-linked hydrophilic network, with the two networks showing no significant cross-reactivity on the detection threshold of nuclear magnetic resonance (NMR) in the resulting composite hydrogel. Herein, we investigate the internal morphology of such simultaneous in situ-gelling IPNs using a combination of SANS (assessing scattering from both networks combined as well as contrast-matching each network individually) and dSTORM super-resolution fluorescence microscopy. In particular, given that the PNIPAM interpenetrating phase is thermosensitive while the PVP IPN is not, the driving force for phase separation between the IPNs is a strong function of the temperature; consequently, we expected to see significant temperature-responsive domain formation in these IPNs. Both SANS and super-resolution fluorescence microscopy indicate phase separation on multiple length scales as well as the presence of a partially mixed internal structure consisting of PNIPAM-rich static inhomogeneities embedded in a clustered PVP-rich phase. Such a morphology could be applied to, for example, thermoresponsive drug delivery or simultaneous delivery of multiple types of active agents that have specific affinities for each of the phases formed in the IPN.

DOI: 10.1021/acsami.7b11637
ACS Appl. Mater. Interfaces 2017, 9, 42179−42191

MATERIALS AND METHODS

Materials. *N*-Isopropylacrylamide (NIPAM; 99%) was purchased from J&K Scientific (Sunnyvale, USA) and purified by recrystallization at 0 °C from toluene, followed by washing with hexanes. Deuterated (d_7) NIPAM (inhibitor-free) was purchased from Polymer Source (Montreal, Canada) and used as received. *N*-Vinylpyrrolidone (99%), acrylic acid (99%) thioglycolic acid (TGA; 98%), glucose oxidase (from *Aspergillus niger*, type X−S, 100−250 units/mg, 65−85% protein content), catalase (from bovine liver, ≥10 000 units/mg, ≥70% protein content), and cysteamine (98%) were purchased from Sigma-Aldrich (Oakville, Canada) and used as received. *N*-Vinylformamide (>96%) was purchased from TCI (Portland, USA) and used as received. 2,2-Azobisisobutyric acid (AIBME, 98%) was purchased from Waterstone and stored under nitrogen. 1-Ethyl-3-(3-dimethylaminopropyl) carbodiimide hydrochloride (EDC, 98%) was purchased from Carbosynth (Berkshire, UK). N-2 aminoethyl maleimide (98%) was purchased from Toronto Research Chemicals (Toronto, Canada). Hydroxybenzotriazole (98%) was purchased from ApexBio (Houston, USA). Adipic acid dihydrazide (97%) was purchased from Alfa Aesar (Tewksbury, USA). The water used was of Milli-Q grade.

Hydrazide-functionalized PNIPAM was modified using Cy5-NHS (Lumiprobe, Hallandale Beach, Florida; 95%) according to established protocols using catalytic amounts of trimethylamine in water.[31] Cy3-maleimide was made by reacting Cy3-NHS (Lumiprobe) with *N*-(2-aminoethyl)maleimide in dimethylformamide. The solvent was evaporated, and the residue was purified via liquid−liquid extraction using dichloromethane and saturated NaCl brine, after which the organic phase was evaporated again to isolate the maleimide-functionalized Cy3 product.

Precursor Polymer Synthesis and Characterization. Hydrazide- and aldehyde-functionalized PNIPAM, both typical protonated polymers (PNIPAM-Hzd and PNIPAM-Ald), deuterated analogues (d_7-PNIPAM-Hzd and d_7-PNIPAM-Ald), and maleimide-functionalized PVP (PVP-Mal) were prepared and characterized (via conductometric titration for Hzd derivatives and ^{1}H NMR for Ald derivatives) as previously described.[30] Thiolated PVP (PVP-SH) was prepared by first copolymerizing *N*-vinyl pyrrolidone and *N*-vinyl formamide (10 mL total monomer in a 4:1 molar ratio) in 55 mL of isopropanol, using 100 mg of AIBME initiator and 160 μL of TGA chain transfer agent. Polymerization was conducted overnight at 60 °C, followed by removal of the solvent under reduced pressure. The product was subsequently redissolved in 1 M NaOH and heated at 70 °C for 24 h to hydrolyze vinyl formamide residues to vinyl amine residues,[32] dialyzed exhaustively (6 × 6 + hour cycles), and lyophilized for storage. Amine content was determined by base-into-acid conductometric titration (0.1 M NaOH titrant, 50 mg polymer in 50 mL of 1 mM NaCl as the sample, Mantech Associates autotitrator). Then, functionalization of the amine residues to form thiols was carried out in water at room temperature using a 1:1.2:3 molar ratio of PVP-*co*-vinyl amine/3-mercaptopropionic acid/EDC, with the reaction run for 2 h under manual pH control, maintaining pH = 4.75. The thiolated product was then dialyzed against dilute HCl (pH 4−5, 6 × 6 + hour cycles), after which the pH was adjusted to pH 7.4, and the solution was immediately lyophilized. The product was stored at −20 °C and was stable in storage for up to 1 month. Whereas conversion is essentially quantitative for the EDC conjugation step based on consumption of free amine groups, residual moisture on the lyophilized polymer can allow disulfide formation even at −20 °C if the polymer is left for an extended period under storage. Polymer molecular weight was measured using gel permeation chromatography (GPC) under configurations chosen according to the solubilities of each polymer tested (see the Supporting Information, Table S1 for a full summary). Table 1 summarizes the properties of the precursor polymers used to prepare all full and semi-IPNs studied herein.

SANS. Neutron scattering experiments were conducted on an NG30 (30 m) SANS instrument at the NIST Center for Neutron Research (NCNR), Gaithersburg, MD, USA. Samples were prepared using the 6 wt % PNIPAM precursor polymer and 9 wt % PVP precursor polymer in phosphate buffered D_2O (or mixed D_2O/H_2O for index matching); the concentrations were chosen such that the storage moduli (G') of the two constituent single networks were approximately equal.[30] The precursor polymers were loaded into separate barrels of a double-barrel syringe (MEDMIX L system, 2.5 mL volume, 1:1 volume ratio between barrels, with mixing baffle), adding the hydrazide/thiol polymers in one barrel and the aldehyde/maleimide polymers in the other barrel (as per Figure 1), and extruded directly into NCNR's custom titanium/quartz sample holders (diameter 19 mm and path length 1 mm). This delivery device was identical to that used for in vivo administration, thus making the morphology results generated directly applicable to the actual use of the hydrogels in a practical application.

Table 1. Properties of Precursor Polymers

polymer	M_w (kDa)	PDI	GPC method	degree of functionalization (mol % functional residues)
PNIPAM-Hzd	19	3.2	basic	20% (titration)
PNIPAM-Ald	23	[a]6.1	DMF	7% (NMR)
PVP-SH	26	2.7	DMF	22% (titration & Ellman's assay)
PVP-Mal	18	2.7	acidic	10% (NMR)
unfunctionalized PVP	26	3.2	basic	N/A
unfunctionalized PNIPAM	9	3.2	DMF	N/A

[a]Magnitude of the polydispersity index (PDI) likely because of interactions between the polymer and column packing material.

Although all cross-linking schemes used result in gelation by vial inversion within seconds to tens of seconds, each sample was allowed to gel for at least 12 h before testing to ensure that equilibrium cross-linking and network formation had occurred prior to analysis. Six groups of samples were assessed: (1) single-network PNIPAM reference (6 wt %), (2) single-network PVP reference (9 wt %), (3) semi-IPN reference consisting of 9 wt % unfunctionalized PVP in 6 wt % PNIPAM (to discriminate the effects of additional polymer being incorporated into the network from the effects of the formation of the IPN), (4) reverse composition of semi-IPN (unfunctionalized PNIPAM in PVP; for the same reason as group 3), (5) full IPN in D_2O (both IPNs visible via SANS), and (6) full IPNs at H_2O/D_2O scattering length density match points for each network to suppress scattering from one of the two constituent networks and independently probe the morphology of each individual network within the IPN phase. Data were collected at sample-to-detector distances of 1 m (high q; at an average acquisition time of 1 min), 4 m (medium q, 3 min), and 13 m (low q; 15 min), using 6 Å wavelength neutrons. Data collected under various q ranges were merged using the NCNR's customized data reduction package of Igor Pro macros.[33,34]

To determine the H_2O/D_2O ratio required to contrast-match a specific network, the theoretical scattering length density for the network was first calculated based on the atomic composition to predict match points of 70:30 D_2O/H_2O to contrast−suppress scattering from the d_7-PNIPAM network and 23:77 D_2O/H_2O to match out PVP scattering. This calculation was next validated by conducting scattering experiments both at the calculated match point as well as at D_2O concentrations of ±10% from the match point for each single-network gel. Total scattering at each of the three solvent compositions was measured, and the D_2O concentration producing zero scattering was determined by regression. On the basis of this experiment, the predicted D_2O/H_2O matching ratios were refined to 73:27 to hide d_7-PNIPAM and 31:69 to hide PVP. Negative controls for each single network collected at the final D_2O/H_2O match points demonstrated greater than order-of-magnitude scattering suppression compared to the corresponding compositions in D_2O (see the Supporting Information, Figure S1 and Tables S2 and S3 for fitting and model parameters).

SANS Data Fitting. Three fitting models were used to assess the scattering curves acquired, with the choice dependent on the type of network analyzed. The classical Porod model[35] (eq 1), which describes

DOI: 10.1021/acsami.7b11637
ACS Appl. Mater. Interfaces 2017, 9, 42179−42191

the scattering from networks without any static inhomogeneities (i.e., domains of varying polymer densities on the length scale accessible to the NG30 SANS), fits well to the thiosuccinimide-cross-linked PVP networks and the room temperature data set for the semi-IPN of PNIPAM chains in a PVP network.

$$I(Q) = \frac{A}{Q^m} + \frac{B}{1 + (\xi\, Q)^n} + C \quad (1)$$

Here, m is the low-q Porod exponent that describes the extent of swelling versus clustering in the network[35,36] (for our data tending to the range characteristic of clustered mass fractals of polymer representing long-range fluctuations of polymer density, predominantly affecting low-q scattering[35]), ξ is the correlation length/mesh size of the gel network (corresponding primarily to the pore size of the hydrogel), n is the Lorentzian exponent characterizing the polymer−solvent interactions at high q values (with values of 5/3 indicating theta solvation, 2 indicating full solvation, and values over 2 attributed to poor solvent interactions,[37] potentially attributable to the high incorporation of residues used for cross-linking and proximity to the volume phase transition temperature (VPTT) in PNIPAM-containing hydrogel formulations), and C is the q-independent, incoherent background.

Alternately, hydrazone-cross-linked PNIPAM networks were best fit by a squared Lorentzian model (eq 2).

$$I(Q) = \frac{A}{(1 + (\gamma Q)^2)^2} + \frac{B}{1 + (\xi Q)^n} + C \quad (2)$$

The first term describes scattering from static inhomogeneities occurring on the larger end of the range of length scales probed by SANS (such as domains of higher polymer concentration within a hydrogel), with γ representing the correlation length scale that is proportional to the average distance between these static features.[38] The second term, describing chain solvation and dynamic fluctuations, is conserved from eq 1.

For noncontrast matched IPNs in which both the PNIPAM and PVP phases show significant scattering, neither the Porod nor the squared Lorentzian function adequately fits the curve shapes. As such, for those materials, a hybrid model (eq 3) was used that sums the contributions from both Porod-type fractal scattering from the PVP phase (term 1) and squared Lorentzian scattering from the PNIPAM phase (term 2), with a common term used to fit the sum of the dynamic contributions from polymer−solvent interactions at the high-q regime from both networks (term 3).

$$I(Q) = \frac{A}{Q^m} + \frac{B}{(1 + (\gamma Q)^2)^2} + \frac{C}{1 + (\xi Q)^n} + D \quad (3)$$

The validity of summing these three terms assumes that scattering events from static domains and clustered regions are noninterfering with each other (i.e., cross-scattering is assumed not to be a factor); the hybrid model's empirical effectiveness at describing scattering from the composite systems appears to support this assumption, which is also consistent with the kinetic orthogonality of the two IPNs.

Super-Resolution Fluorescence Microscopy. To corroborate the structural information inferred from neutron scattering fitting, dSTORM microscopy was used to track the segregation of fluorescently labelled PNIPAM and PVP in IPNs prepared from the two kinetically orthogonal networks. PNIPAM-Hzd was labelled with ∼0.005 mol % (on a total monomer residue basis) Cy5-NHS, whereas PVP-SH was labeled with ∼0.05 mol % of a maleimide derivative of Cy3; the slightly higher labeling density used for PVP-SH is attributable to the differing brightness of the two fluorophores in the imaging buffer (with Cy5 providing greater overall emission due to its higher quantum yield, higher number of cycles, and higher survival after irradiation relative to Cy3), but is still far below an amount that would significantly alter the degree of cross-linking of the hydrogel. In both cases, the average labelling is less than one fluorophore per polymer chain.

Thin-layer hydrogels for imaging were fabricated on microscope slides by spin-coating freshly mixed precursor polymer solutions immediately following mixing. PNIPAM networks produced thin hydrogel sheets at the same 6 wt % concentration used in SANS sample preparation, but the greater viscosity of the PVP precursors required dilution to 3.5 wt % to sufficiently spread the precursor mixture via spin-coating. Although the possible effect of this lower concentration on the phase structure of the IPN cannot be ruled out, it should be noted that the difference in the gelation time between this concentration and the 9 wt % concentration used for the SANS studies is not particularly significant; indeed, even at the lower concentration, the PVP network still gels within <10 s. Also, solvent evaporation during the spin-coating process will affect the precursor polymer concentration and inevitably accelerate the gelation time of both the polymers during the spin-coating process. As such, while it is recognized that these differences in sample preparation between the SANS and dSTORM measurements may pose some impact in terms of the absolute comparisons between the two methods, the relative gelation speeds of the two networks and the chemical nature of the two networks are similar in both cases, such that the features derived from phase separation are expected to be similar in both types of samples.

Polymer precursor solutions were mixed for 5 s, spotted at a 20 μL volume on a plasma-cleaned MaTek glass-bottomed Petri dish, and spun for 60 s at 1500 rpm for PNIPAM single networks or 4000 rpm for the more viscous PVP and IPN precursor mixtures. The gels were stored in 50 mM Tris/10 mM NaCl buffer (pH 8) until imaging. The samples were then transferred to Tris buffer also containing 10 wt % glucose, 100 mM cysteamine, 84 units/mL glucose oxidase, and 510 units/mL catalase 5 min before image collection. The samples were imaged using a Leica CTR6000 inverted fluorescence microscope with a Leica 100×, 1.47 numerical aperture oil immersion objective. Illumination was achieved with solid-state lasers housed within a spectral integrated light engine that controls light powers and couples laser lines (405, 488, 561, and 647 nm) to a single output channel. The laser light was coupled to the objective using the spectral Borealis module, and the samples were imaged in the wide-field epifluorescence mode. Emission light was directed toward the cameras using a multiline dichroic mirror and split into separate color channels using a dichroic mirror with a cutoff of 640 nm. The emission light was filtered with the appropriate color filters (40−60 nm bandwidth), and the images were simultaneously captured using two iXon Ultra DU-897U cameras in the single-molecule mode (17 MHz readout mode, 3.30 μs vertical clock speed, electron-multiplying mode) with a frame size of 256 × 256 pixels (24.6 μm × 24.6 μm field of view) and a binning mode of 1. A dSTORM acquisition was obtained by recording a 10 000 frame video (30 ms exposure) and illuminating the sample with 70−100% laser power of the appropriate wavelength for the specific dye being probed (565 nm for Cy3 and 647 nm for Cy5). Short (2−3 s) bursts of 405 nm irradiation at 2−20% illumination power were used to reactivate the fluorophores (predominantly Cy5) as needed.

To image the samples as a function of the temperature, PNIPAM single network and PNIPAM/PVP IPN hydrogels were spin-coated on 40 mm, no. 1.5 glass slides that were mounted onto an FCS2 Bioptechs microfluidic heating chamber (Bulter, Pennsylvania, USA) filled with Tris buffer (pH 8.0). The imaging buffer was then introduced into the chamber, and the sample and microscope objective were heated to either 25 or 37 °C using the microfluidic chamber and a Bioptechs objective heater, respectively. dSTORM acquisition and data analysis were performed as described above.

Image stacks were cropped to a time point of reasonable fluorophore densities. Localization-fitting analysis was accomplished using the ThunderSTORM ImageJ plugin[39] by applying a B-spline wavelet filter, approximating molecular positions through the local maximum method and calculating subpixel localizations by fitting a two-dimensional integrated function using the weighted least squares method. To avoid artifacts, localization fits with sigma below 75 nm or above 175 nm were discarded, given that the theoretical spread of the point spread function should be ca. 100 nm (eq 4), where λ is the emission wavelength and NA is the numerical aperture of the objective. Emitters with a photon count greater than 3000 were also omitted, as this fell significantly out of the range of photon counts for

DOI: 10.1021/acsami.7b11637
ACS Appl. Mater. Interfaces 2017, 9, 42179−42191

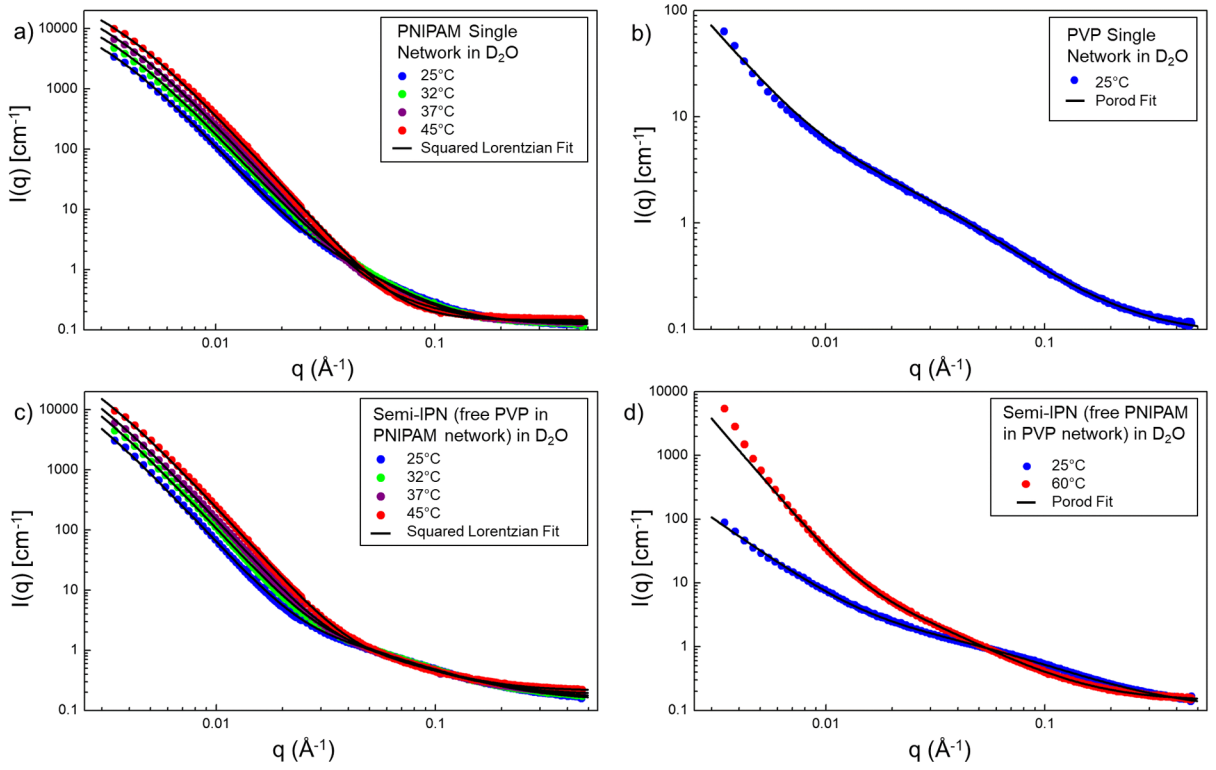

Figure 2. Scattering profiles for single networks and semi-IPNs in 10 mM phosphate buffered saline prepared in D_2O: (a) hydrazone-cross-linked PNIPAM single-network hydrogel as a function of temperature; (b) thiosuccinimide-cross-linked PVP single-network hydrogel (25 °C); (c) free PVP in a hydrazone-cross-linked PNIPAM network semi-IPN network hydrogel (PVP-in-PNIPAM) as a function of temperature; (d) free PNIPAM in a thiosuccinimide-cross-linked PVP semi-IPN network hydrogel (PNIPAM-in-PVP) as a function of temperature.

individual localizations and could represent overlapping emitters. Localizations were further refined by using a bandpass filter for uncertainties in the 5−30 nm range, which removed localizations corresponding to multiple overlapping emitters (low localization uncertainty) or corresponding to noise or rapidly bleaching molecules (high localization uncertainty). The application of these filtering steps did not change the overall structure of the reconstructed images, but ensured that all localizations used in the reconstruction corresponded to individual emitters.

$$2.36\sigma \approx \text{fwhm} = d = \frac{\lambda}{2\text{NA}} \tag{4}$$

Sample drift was corrected using the cross-correlation method, and the super-resolution image was rendered with a magnification factor of 5 (19.2 nm pixel size) and slightly blurred with a lateral shift of 2 pixels.

RESULTS AND DISCUSSION

SANS on Single-Network and Semi-IPN Hydrogels. We have previously shown that the thiosuccinimide-cross-linked PVP network and the hydrazone-cross-linked PNIPAM network form in a kinetically orthogonal manner, with no significant cross-reactivity occurring between the networks to produce an IPN structure.[30] These IPN systems showed a ∼3-fold enhancement of the shear storage modulus compared to either constituent single network in isolation, as well as slower and more reversible thermal transitions and substantially enhanced resistance against hydrolytic degradation.[30] All these properties are consistent with the creation of an IPN structure in which the thermoresponsive/degradable PNIPAM phase and the nonthermoresponsive/nondegradable PVP phase are intimately mixed. However, no clear evidence of the degree of phase mixing was presented, that is, information essential to rationally engineering this chemistry for creating hydrogels with targeted properties. The SANS and dSTORM analyses conducted in this paper aim to develop these required structure−property correlations.

Both the PNIPAM-hydrazone and PVP-thiosuccinimide networks gelled rapidly upon mixing, within 2−10 s for the PVP-thiosuccinimide network and 90 s for the PNIPAM-hydrazone network; gelation of the IPN was governed by the faster gelling PVP phase, with gelation observed within 5 s. Concurrent to gelation, the appearance of the gel converts from fully transparent in the precursor solutions to opaque on a time scale commensurate with the kinetics of gelation of the fastest component of the IPN system (PVP-thiosuccinimide at the polymer concentrations used), suggesting the formation of inhomogeneities on the length scale of visible light. A similar switch in opacity was observed in semi-IPN hydrogels, regardless of which polymer constituted the entrapped polymer phase, again suggesting phase sequestration in these materials during gelation that could be probed using SANS techniques.

SANS analysis on the PVP and PNIPAM single-network reference gels showed significant differences in the nanostructure. In particular, the PNIPAM single-network control exhibits a tendency toward a plateau at low q (Figure 2a), whereas the PVP single-network control shows a straight power law trend at low q (Figure 2b).

Semi-IPNs prepared with both free PVP in a PNIPAM network (Figure 2c) and free PNIPAM in a PVP network (Figure 2d) show the same trends as their corresponding single-network profiles, with an upward inflection observed in the PVP network semi-IPN and a decreasing slope observed in the PNIPAM network semi-IPN at low q. This demonstrates

DOI: 10.1021/acsami.7b11637
ACS Appl. Mater. Interfaces 2017, 9, 42179−42191

Table 2. Summary of Key Fitting Parameters for SANS Data

	T (°C)	model used	Porod exponent	squared Lorentzian correlation length (nm)	fluid term correlation length (nm)	fluid term exponent
PVP single network in D_2O	25	Porod	2.4		3.7	1.7
semi-IPN (PVP in PNIPAM network) in D_2O	25	Porod	2.4		2.1	1.6
	60		4.0		4.8	1.9
PNIPAM Single Network in D_2O	25	squared Lorentzian		37	3.0	2.3
	32			36	2.7	2.4
	37			36	1.1	3.0
	45			35	1.0	3.1
semi-IPN (PVP in PNIPAM network) in D_2O	25	squared Lorentzian		61	2.3	1.8
	32			58	2.3	1.9
	37			55	1.7	2.1
	45			51	1.2	2.3
IPN in D_2O	25	hybrid	3.5	12	4.4	1.9
	32		3.4	8.3	3.8	1.9
	37		3.5	8.2	2.1	2.0
	45		3.4	8.2	1.3	2.4
IPN (PNIPAM scattering suppressed, at 73 D_2O/27 H_2O)	25	Porod	2.8		1.5	2.4
	32		2.8		1.6	2.3
	37		2.7		1.8	1.9
	45		2.7		2.0	1.7
IPN (PVP scattering suppressed, at 31 D_2O/69 H_2O)	25	squared Lorentzian		**64**	**19**	**2.2**
	32			**52**	**8.8**	**2.7**
	37			**45**	**7.7**	**3.2**
	45			**40**	**7.5**	**4.1**
IPN (PNIPAM scattering suppressed, at 73 D_2O/27 H_2O)	25	hybrid	2.8	22	4.8	1.9
	32		2.8	21	4.5	1.9
	37		2.7	20	4.1	1.9
	45		2.7	18	3.5	2.0
IPN (PVP scattering suppressed, at 31 D_2O/69 H_2O)	25	hybrid	2.7	53	6.9	2.2
	32		2.7	46	7.1	2.7
	37		2.8	45	7.2	3.7
	45		2.6	39	8.8	4.0

that the cross-linked phase is the primary influence on the low-q scattering profile of the semi-IPNs, as is expected given that the low-q scattering arises from larger network features. The Porod model (derived for networks characterized as mass fractals that lack the presence of static inhomogeneities[36]) fits the PVP scattering profile well, but fails to converge when tested against PNIPAM network scattering plots. By contrast, the squared Lorentzian model (designed to model such static inhomogeneities or domains[38,40]) is able to accurately capture the trend toward a plateau seen at low q in PNIPAM networks but cannot converge on the power law-type curves characteristic to PVP networks. Thus, PNIPAM-only networks appear to consist of domains of static inhomogeneities, whereas PVP networks can be described as a mass fractal network (at least within the accessible length scale; it is possible static structures occur within the PVP network on larger length scales than what NG30 SANS can probe). See also the Supporting Information, Tables S4−S7 and Figures S2−S5 for model fit parameters and comparisons of individual raw scattering data to model fits for single networks and semi-IPNs.

The correlation length (proportional to the interdomain spacing) in the PNIPAM single network decreases slightly from 37 to 35 nm with heating from 25 to 45 °C (Table 2). However, the semi-IPN consisting of free PVP inside a PNIPAM network exhibits a decrease in the correlation length from 61 to 51 nm over the same temperature range (Table 2). Although a decrease in the correlation length was expected for both these samples, given the deswelling behavior of PNIPAM above its lower critical solution temperature, the greater relative decrease of the correlation length observed in the semi-IPN was somewhat surprising, given that our previous work showed bulk volume phase transitions in the semi-IPN formulation that were smaller than those in the single network.[30] We hypothesize that the observed trend in the correlation lengths may result from a combination of domain shrinkage and changes in the interdomain spacing, with the semi-IPN more effectively sequestering water, given the capacity of the non-cross-linked PVP to move within the networks and thus maintain highly locally hydrated microdomains (particularly at temperatures above the VPTT of PNIPAM).

The Porod exponent (for which n = 2 represents Gaussian chains and n = 3 represents collapsed clusters[35]) was an intermediate 2.4 for the PVP single network and a more clustered 2.7 for the PNIPAM-in-PVP semi-IPN network (both

DOI: 10.1021/acsami.7b11637
ACS Appl. Mater. Interfaces 2017, 9, 42179−42191

assessed at 25 °C, below the PNIPAM phase transition temperature; Table 2). This suggests that the presence of PNIPAM polymers within the composite drives the structure toward additional clustering even when PNIPAM is not cross-linked, suggesting at least a moderate driving force for phase separation between the two polymers.

SANS on Full IPN Hydrogels. IPN hydrogels in which both PNIPAM and PVP are cross-linked showed neither of the inflection features at low q that correlated with the two previous fitting models. Instead, scattering from IPNs followed a smooth curve, with a broad and shallow peak overlapping at approximately $q \approx 0.015$ Å^{-1} developing at a higher temperature (Figure 3a). Neither fitting model was able to capture both this small peak and the smooth trajectory of the low-q segment of the scattering plot. Reasoning that the scattering in the IPN would be a cumulative function of the contributions from the two constituent networks, a hybrid model (eq 3) which combines the scattering contributions from both a Porod function (for the PVP network) and a squared Lorentzian function (for the PNIPAM network) was used to fit the full IPN data (see also the Supporting Information Table S8 and Figure S6 for the raw scattering data and hybrid fits using eq 3 for all IPN samples at all temperatures tested).

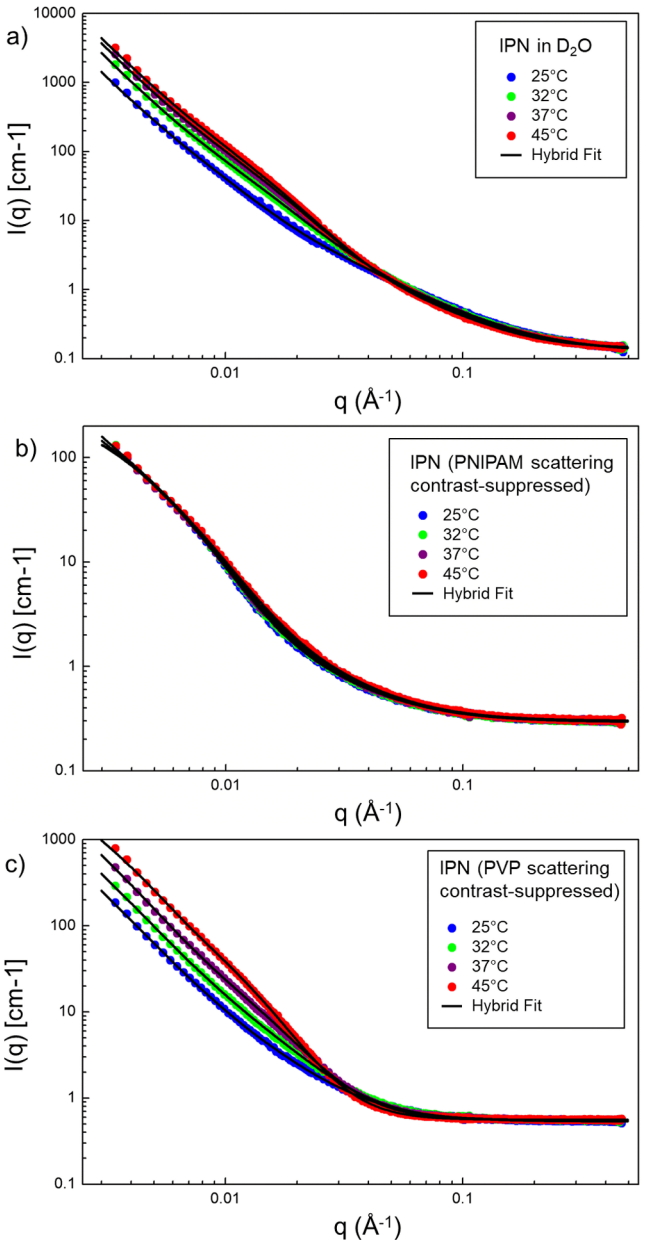

Figure 3. Scattering profiles for IPN hydrogels: (a) PVP/PNIPAM IPN hydrogels as a function of temperature in D_2O; (b) temperature response of PVP/d_7-PNIPAM IPN hydrogels in which the PNIPAM network is index matched out (at 31:69 D_2O/H_2O); (c) temperature response of PVP/d_7-PNIPAM IPN hydrogels in which the PVP network is index matched out (at 73:27 D_2O/H_2O).

In general, the Porod component exponent was ~3.4 in the best set of fit values; although physically possible in systems that have experienced extreme clustering/collapse within certain scattering domains, however, this number is significantly higher than that previously observed in hydrogels. Correspondingly, the squared Lorentzian correlation length decreases from 12 to 8 nm with increasing temperature (Table 2), suggesting significantly smaller average distances between the static inhomogeneities than in the PNIPAM single network.

Although the temperature-dependent peak at $q \approx 0.015$ Å^{-1} provides compelling evidence that PNIPAM still drives static inhomogeneity formation and thermal collapse, the hybrid model is limited in its ability to quantitatively distinguish the scattering features attributable to the structure of each network. For example, the squared Lorentzian component of the hybrid model accounts for less than half of the total scattering intensity in the low-q portion of the scattering profile at all temperatures studied, despite the fact that the single-network controls indicated that PNIPAM scattered significantly more strongly than PVP at the low-q range (see the Supporting Information Figure S6 for comparisons of the relative contributions of the Porod and squared Lorentzian components to the hybrid fits for IPNs in D_2O).Although the hybrid fits do give some insight into the structures formed in the IPN, further experimentation was deemed necessary to clarify the individual network structures inside the IPN.

To more clearly compare the structures formed by each polymer in the single-network gels relative to the IPNs, SANS experiments with contrast-matched samples were performed by preparing hydrogels with the deuterated analogue of PNIPAM to selectively examine scattering contributions from each network. Figures 3b (PNIPAM suppressed) and 3c (PVP suppressed) show the index-matched SANS profiles for each network over the full 25−45 °C temperature range. In addition to the effective zeroing of the overall scattering intensity observed in the single-network hydrogel controls at the relevant solvent match points (Supporting Information, Figure S1), the temperature dependence of both index-matched samples further suggests success in isolating the scattering attributable to each network; no significant change in the scattering profile is noted as a function of temperature when the d_7-PNIPAM phase was suppressed, whereas a clear temperature response was observed when the PVP phase was suppressed (Figure 3b,c).

With d_7-PNIPAM matched out (Figure 3b), the Porod model achieves reasonable fits with an exponent averaging 2.7 (Table 2; also see the Supporting Information, Figure S7 and Table S9 for raw data and complete fitting parameters). It should however be noted that the Porod model does not fully fit the small but distinct peak overlapped onto the Porod profile at $q \approx 0.007$ Å^{-1} (Figure 3b), an inflection that was not observed in the PVP single-network control hydrogel (Figure 3b). This feature could be interpreted either as an interference

DOI: 10.1021/acsami.7b11637
ACS Appl. Mater. Interfaces 2017, 9, 42179−42191

arising from incomplete suppression of the PNIPAM scattering (unlikely because of the effective suppression shown in the Supporting Information, Figure S1) or as an evidence for the incorporation of a minority fraction of PVP into the PNIPAM-rich static domains that are hidden at this contrast point. The latter interpretation is consistent with the previously noted lower-than-anticipated contribution of the squared Lorentzian term in the low-q scattering regime for IPN samples collected in D_2O.

With PVP matched out, the scattering profile of the remaining d_7-PNIPAM network retains the temperature dependence normally associated with PNIPAM (Figure 3c) and can be fit using the squared Lorentzian model previously found to effectively fit the PNIPAM single-network hydrogel, with the correlation length decreasing from 64 nm at 25 °C to 40 nm at 45 °C (Table 2; see also the Supporting Information, Figure S8 and Table S10 for raw data and full model fitting parameters). However, unlike with single-network PNIPAM hydrogels, no low-q plateau is observable in the accessible q range for the index-matched samples. Obtaining reasonable squared Lorentzian fits also depends on allowing the second Lorentzian term from eq 2, representing fluid effects, to assume correlation lengths significantly larger than those seen in the PNIPAM single-network control (Table 2; also see the Supporting Information, Tables S6 and S10 for a more direct comparison). The correlation length is typically interpreted to be proportional to the network mesh size; whereas it is physically possible for PVP interpenetration to increase the PNIPAM mesh size relative to the single-network control, the magnitude of the increase suggests that this classical interpretation of the correlation length may not be physically valid within an IPN network (particularly one in which one of the interpenetrating phases is rendered functionally invisible during the SANS analysis).

As such, both contrast-suppressed samples show some features inconsistent with the single-network controls of those same networks; specifically, the small peak at $q \approx 0.007$ $Å^{-1}$ in Figure 3b can be interpreted as some fraction of the PVP component entrapped in the (index-matched) PNIPAM-rich domains, whereas the suppression of the plateau feature seen in PNIPAM single networks within the studied q range in Figure 3d can be interpreted as mixing of some of the d_7-PNIPAM into (index-matched) PVP clusters. To test this interpretation, the hybrid model was used to fit the contrast-matched IPN data, looking for evidence of some of each network type being "dragged" into the structural configuration expected for each index-matched IPN network. Scattering curves for IPN networks in which the d_7-PNIPAM phase was suppressed fit well to the hybrid model (Figure S9 and Table S11; fit traces also shown on Figure 3b), showing considerable improvement in the fitting error metrics compared with the unmodified Porod model. Specifically, inclusion of the squared Lorentzian term facilitates an accurate fitting of the small feature at $q \approx 0.007$ $Å^{-1}$. As expected, the Porod contribution (used to fit the PVP single-network gel) dominated scattering fits in this system, with the exponent virtually unchanged (at 2.75) across all temperatures (Table 2). Across the temperature series, the contribution of the Porod component to the total hybrid fit increases from low to high temperature, whereas the importance of the squared Lorentzian term shrinks (see Supporting Information, Figure S9), consistent with the reduced fluidity of the network as the (invisible) PNIPAM phase shrinks around the (visible) PVP phase. Furthermore, the squared Lorentzian component correlation length shifted from 22 to 18 nm as the temperature was increased from 25 to 45 °C (Table 2). Compared to the control scattering profile collected from a d_7-PNIPAM single network at its match point, in which the residual scattering lacked temperature dependence, the thermal dependence observed in this correlation length strongly indicates that the small feature at $q \approx 0.007$ $Å^{-1}$ arises at least partly because of the entrapment of some PVP into the PNIPAM-dominated static inhomogeneities that are physically compressed by the temperature-responsive collapse of the surrounding PNIPAM network.

The hybrid model is also successful at modeling the scattering profiles of IPNs in which the PVP network is matched out (Figure 3c and Supporting Information, Figure S10 and Table S12). This is particularly true in the low-q linear region of the scattering plot, for which the squared Lorentzian model assumed inflection points at q values below the experimental range. With increasing temperature, the correlation length parameter in the Lorentzian component of the hybrid model decreases from 53 to 39 nm, considerably closer to the values obtained in the PNIPAM single-network fits (37–35 nm) than the parameter values extracted from using the squared Lorentzian model on the same index-matched IPN data (64–40 nm) (Table 2). Interestingly, the Porod component (with exponents in the 2.6–2.8 range) contributes to a surprising fraction of the overall scattering intensity observed at lower temperatures, although the growing Lorentzian contribution at higher temperatures (as the PNIPAM network collapses) reduces the importance of the Porod contribution to the fit (Supporting Information, Figure S10). Mechanistically, given the approximately 90 s gelation time for hydrazone cross-linking in the single-network PNIPAM hydrogels, this result is physically consistent with the possibility of significant mixing of the PNIPAM-Hzd and PNIPAM-Ald prepolymers into the PVP-rich clustered fractal phase prior to full gelation of the PNIPAM network, followed by physical entrapment of these precursor polymers in this mixed state. This interpretation is also consistent with the Porod component of the hybrid fits of total IPN scattering from D_2O (when both networks are visible) contributing to a more significant fraction of the fit than expected from the summation of the single-network scattering intensities; that is, mixing with the PVP network appears to be partially disrupting the static inhomogeneity formation by the PNIPAM network.

Of note, in the corresponding semi-IPN scattering profiles (Figure 2c,d), the hybrid model is not necessary to fit the scattering curves. Whereas mixing may occur similarly on the time scale of the gelation of one network in the semi-IPN hydrogels, the entrapped free polymer maintains sufficient mobility to allow for subsequent phase separation in a way not possible in the fully cross-linked/entangled IPN samples, effectively reversing this mixing over time prior to the SANS analysis.

It should be noted that our choice of models differs from most previous SANS analyses on acrylamide-based hydrogels, which typically use an exponentially decaying static component[41,42] (e.g., a Guinier function[43]) in combination with the Lorentzian dynamic component also used in our fits. Relative to these previous papers, our samples exhibit a much higher low-q scattering (indicative of higher inhomogeneity) and less-defined features and require the use of different models to effectively fit; indeed, attempts to fit both single networks and IPN networks using the Guinier–Lorentzian functions typically

DOI: 10.1021/acsami.7b11637
ACS Appl. Mater. Interfaces 2017, 9, 42179–42191

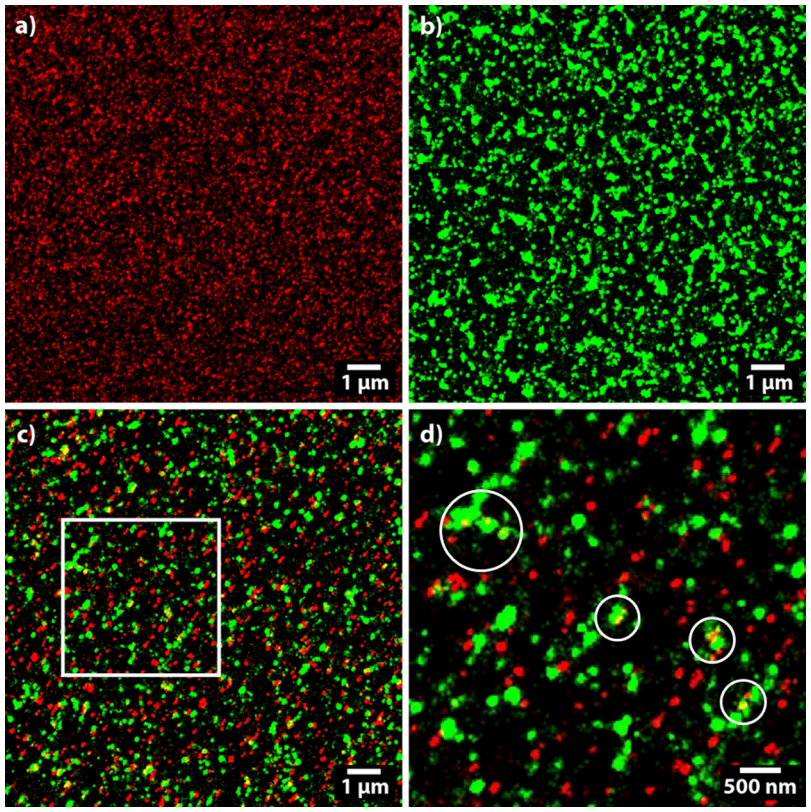

Figure 4. Reconstructed dSTORM images of Cy3-PVP/Cy5-PNIPAM single network and IPN hydrogels: (a) PNIPAM single network; (b) PVP single network; (c) PVP/PNIPAM IPN; (d) magnification of the inset region of IPN, highlighting several instances of PNIPAM domains within larger PVP features (circled).

used for PNIPAM hydrogels failed to capture key features in both the low-q and high-q regimes (see Supporting Information, Figure S11). We attribute this difference to the very different mechanisms by which the gels are fabricated. In this work, hydrogels are formed based on rapid cross-linking of functionalized oligomeric materials at room temperature and include two different backbones and four functionally different polymers (hydrazide/aldehyde functionalized PNIPAM and thiol/maleimide functionalized PVP), all of which have some potential to phase-separate. Relative to free radical copolymerization from monomeric units, mixing-induced gelation of an IPN would be expected to result in significantly more heterogeneous networks; given that the starting materials are themselves polymers (and thus have mass transfer/mixing limitations), the gelation rate is very fast (here typically <1 min, such that diffusive mixing does not happen to the same degree during the reaction), and there are kinetic driving forces for phase separation among the starting materials themselves. However, even in that context, contrast-matching shows that each constituent network has a defined SANS signature that can be fit by a physically meaningful SANS scattering function. As such, while the inherent heterogeneity of the samples may obscure the extraction of more detailed information (or rather, more detailed information is not extractable from the fits because of the heterogeneity of the network), the quality of fits achieved for each network and the consistent physical relevance of those fits make us confident in our interpretation of the data.

Super-Resolution Fluorescence Microscopy Analysis. To further validate our interpretation of the phase structure of these IPN hydrogels, super-resolution fluorescence microscopy was performed on PVP/PNIPAM IPN hydrogels. The dSTORM technique probes length scales significantly larger than SANS, with each reconstructed pixel in the images representing 20 nm in our configuration; as such, the dSTORM measurements should be viewed as complementary to SANS, allowing us to better understand the microscale morphology of these simultaneous IPN structures in which phase separation can occur on multiple length scales. In addition, given the need to prepare thin-film samples to minimize the background in the dSTORM analysis, a spin-coating sample preparation technique was used as opposed to extrusion through the static mixer. As such, we recognize that dSTORM probes the gel morphology on a different length scale and cannot be definitively compared to the SANS results. However, even in this context, the images show generally similar tendencies for each network type, as suggested by the SANS experiments, and the larger feature sizes accessible by dSTORM allow us to examine the homogeneity of the network intermixing across a wider range of characteristic length scales than accessible by SANS alone. The Cy5-PNIPAM network (Figure 4a) forms smaller and more distributed domains or clusters consistent with the observed formation of smaller static inhomogeneities in the network structure from SANS; correspondingly, the Cy3-PVP network (Figure 4b) appears to organize in clusters with a significant distribution of sizes and shapes, as would be expected if the conclusion from the SANS data that the PVP network forms predominantly clustered mass fractals held true on larger length scales. Note that the necessity of using a higher labelling density of Cy3 (on PVP) than Cy5 (on PNIPAM) to achieve a good signal-to-noise ratio on each channel for each frame of the acquisition stack does have potential to bias the result in terms of PVP only appearing to show larger clusters simply because it

DOI: 10.1021/acsami.7b11637
ACS Appl. Mater. Interfaces 2017, 9, 42179−42191

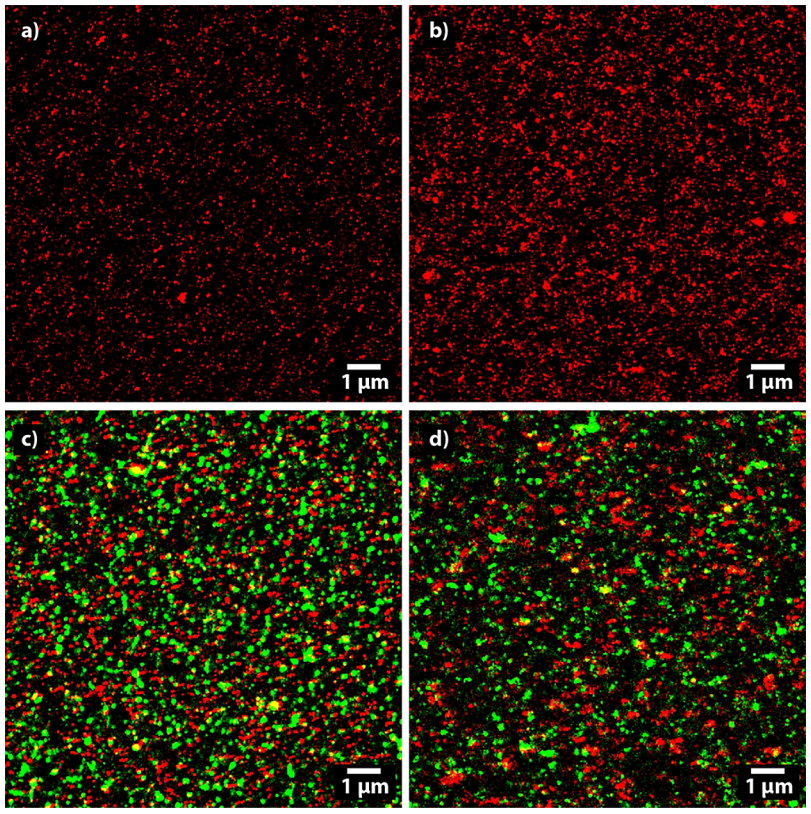

Figure 5. Reconstructed dSTORM images of thermal phase transitions in PNIPAN single networks (a,b) and PNIPAM/PVP IPNs (c,d): (a) Cy5-PNIPAM single network at 25 °C; (b) Cy5-PNIPAM single network at 37 °C; (c) Cy5-PNIPAM/Cy3-PVP IPN at 25 °C; (d) Cy5-PNIPAM/Cy3-PVP IPN at 37 °C.

is more heavily labelled. However, the spaces between clusters with either no fluorophore signal or scattered, individual fluorophore signals are also more pronounced in Figure 4a (Cy5 labeled) than in Figure 4b (Cy3 labeled). As such, this strong cluster-to-background contrast in both reconstructed localization plots suggests that the observed difference in the cluster size and the spatial frequency accurately reflects the underlying features of the two networks.

The IPN sample (Figure 4c) appears to preserve the characteristic features of both single-network samples, with generally discrete smaller Cy5-PNIPAM domains in a field of larger, extended, and to some extent interconnected Cy3-PVP clusters. Interestingly, whereas the majority of the signals from each network are discrete (as would be expected in a conventional IPN in which the two interpenetrating phases are fully phase-separated), there is also clear evidence of PVP clusters containing signals associated with PNIPAM (red circles in Figure 4d). However, relatively few of the discrete PNIPAM structures show evidence of any smaller clusters of PVP colocalized. Indeed, at high magnifications of the IPN image (Figure 4d), only a minority of the larger Cy3-PVP clusters contain smaller pockets of overlapping Cy5-PNIPAM, but the discrete Cy5-PNIPAM domains much less frequently contain overlapped Cy3-PVP signals (i.e., it is more common to see large Cy3-PVP clusters with smaller colocalizations of Cy5-PNIPAM than vice versa). Stacking in the vertical direction was deemed unlikely to account for the observed instances of overlapping structures because of structures of both labelling types being found consistently in the same focal plane.

Such observations are consistent with the SANS data that suggested the presence of PVP-rich mass fractal clusters containing a significant fraction of intermixed PNIPAM as well as the index-matched profiles of SANS fitting, in which the scattering plot of IPNs that were matched to hide PVP while showing d_7-PNIPAM suggests a reduced scattering contribution from static domains as compared to PNIPAM single-network controls (Figure 3c). If the pattern of PNIPAM incorporation into PVP clusters seen on the mesoscale with dSTORM imaging also extends to the length scale probed by SANS, this suggests that the effects seen in SANS might result not from a generally consistent extent of mixing throughout the network but rather from the frequency of PNIPAM-rich domains occurring within larger PVP clusters versus in isolation.

To evaluate the impact of the PNIPAM thermal transition on domain segregation using dSTORM, spin-casted samples were imaged at 25 °C [T < VPTT of PNIPAM] and 37 °C (T > VPTT of PNIPAM), with the results shown in Figure 5. In PNIPAM single-network samples (Figure 5a,b), domains were not observed to shrink laterally with increasing temperature, a result we attribute to the strong adhesion between the PNIPAM single-network gel and the glass substrate. However, the observed localizations were concentrated more strongly in the focal plane, with out-of-plane unfocused localizations significantly reduced and the overall intensity of the observed fluorescence at the focal plane increased upon heating. These observations are strongly indicative of contraction in the thickness dimension. The distribution of cluster sizes also shifts toward larger groupings, suggesting aggregation of domains. The IPN system, in contrast, showed a significantly less indication of contraction to bring more fluorophores into the focal plane upon heating (Figure 5c,d), consistent with our earlier results that PNIPAM-driven VPTT transitions in the

DOI: 10.1021/acsami.7b11637
ACS Appl. Mater. Interfaces 2017, 9, 42179−42191

IPN are inhibited by the IPN.[30] Furthermore, the distribution of PNIPAM domain sizes is broadened at 37 °C, with increases in the populations of clusters, both larger and smaller than the room temperature average. This observation suggests that clusters are shrinking overall, with inhibited mobility due to the hydrophilic PVP network preventing some of the deswollen PNIPAM clusters from participating in the larger aggregates that would be thermodynamically favorable. The dSTORM result is also consistent with the SANS result of increased scattering intensity at higher temperatures, related to the formation of at least a fraction of larger domains.

This work represents, to our knowledge, the first instance of contrast-matching SANS and super-resolution optical techniques being combined to probe the meso- and nanoscale structure of a hydrogel composite. By combining the conventional SANS, the index-matched SANS in which each network is individually visible, and the dSTORM super-resolution fluorescence microscopy, a coherent picture of the structure of these hydrazone-cross-linked PNIPAM/thiosuccinimide-cross-linked PVP IPN hydrogels emerges. Phase separation appears to occur faster than the timescale of gelation, leading to the creation of interlocking networks that form relatively (but not totally) independently to create nanoscale morphologies similar to those observed in a corresponding single-network gel (i.e., analogous to a conventional IPN system). However, the relatively fast gelation kinetics appear also to lead to the entrapment of a fraction of one phase in another, primarily some PNIPAM (the slower gelling component of the gelling pair) inside the (faster-gelling) PVP-rich fractal-like domains. This morphological picture is also highly consistent with the observed physical properties of these hydrogels, with the enhanced mechanics, suppressed thermoresponsivity, and inhibited degradation observed,[30] all consistent with the combination of interlocking networks that also contain some degree of entrapment of the temperature-responsive/degradable PNIPAM phase into the nontemperature-responsive/nondegradable PVP phase. This domain structure may present significant interest in the context of controlled release from these networks, given that drugs with a high affinity for the PNIPAM phase (particularly if loading is done at temperatures above the phase transition of the PNIPAM phase) may be released at two independent rates: one corresponding to release from the phase-separated PNIPAM network and another corresponding to release from the PNIPAM phase entrapped inside the PVP clusters. The fully injectable nature of this particular IPN, in contrast to previously reported IPNs, also makes it more amenable to potential translation to biomedical applications if the anticipated dual-phase release kinetics were achieved, as surgical implantation would not be required. Understanding this morphology may also give insight into the mechanics of these IPNs, as the minority population of interlocked structures inside a largely phase-separated matrix suggests a significant role for these mixed clusters in the observed enhancement of mechanical strength of the IPN relative to the two single networks alone.[30]

CONCLUSIONS

SANS and super-resolution fluorescence microscopy have been applied to investigate the internal morphologies of fully injectable IPN hydrogels comprised of thiosuccinimide-cross-linked PVP and thermoresponsive hydrazone-cross-linked PNIPAM. Investigations on both the nanoscale (SANS) and mesoscale (dSTORM) suggest phase segregation into discrete populations of predominantly PNIPAM, predominantly PVP, and mixed domains, with the trend of PVP-rich structures containing more PNIPAM than vice versa, apparent across both scales that were assessed. Such a morphology is consistent with the relative kinetics of gelation and phase separation in these hydrogels, as gelation can effectively freeze the diffusion of a fraction of one polymer out of a phase rich in the other polymer before complete phase separation can occur; by contrast, for the semi-IPN controls in which one network remains un-cross-linked, no significant mixed domains were visible through SANS fitting. We anticipate that understanding this domain structure can be used to optimize the drug release kinetics and mechanical enhancements possible with such fully injectable IPN systems. Furthermore, this work suggests that the combination of super-resolution microscopy and SANS has significant potential to better understand the internal morphologies of IPN hydrogels across multiple length scales and thus design more effective IPN structures targeted to applications.

ASSOCIATED CONTENT

Supporting Information

The Supporting Information is available free of charge on the ACS Publications website at DOI: 10.1021/acsami.7b11637.

SANS raw data and fitting plots for all samples tested (PDF)

AUTHOR INFORMATION

Corresponding Author

*E-mail: hoaretr@mcmaster.ca.

ORCID

Richard J. Alsop: 0000-0003-0563-0063

José Moran-Mirabal: 0000-0002-4811-3085

Todd Hoare: 0000-0002-5698-8463

Notes

The authors declare no competing financial interest.

ACKNOWLEDGMENTS

The Natural Sciences and Engineering Research Council of Canada (NSERC, CREATE-Integrated Design of Extracellular Matrices 398058, Discovery Grants RGPIN 356609 and RGPIN 418326), the Ontario Ministry of Research and Innovation (Early Researcher awards ER09-06-185 and ER14-10-108), and the Canada Foundation for Innovation—Leader's opportunity Fund (award 29898) are gratefully acknowledged for the financial support. M.B. is supported by an NSERC—Canada Graduate Scholarship—Masters Program. This work utilized facilities supported in part by the National Science Foundation under agreement no. DMR-0944772. We acknowledge the support of the National Institute of Standards and Technology, US Department of Commerce, in providing the neutron facilities used in this work. We also thank Yimin Mao, NCNR instrument scientist, for the NG30 SANS and for supervising our research visit as well as all other NCNR staff who helped facilitate our experiments.

REFERENCES

(1) Hoare, T. R.; Kohane, D. S. Hydrogels in Drug Delivery: Progress and challenges. *Polymer* **2008**, *49*, 1993–2007.

(2) Naficy, S.; Kawakami, S.; Sadegholvaad, S.; Wakisaka, M.; Spinks, G. M. Mechanical Properties of Interpenetrating Polymer Network

DOI: 10.1021/acsami.7b11637
ACS Appl. Mater. Interfaces 2017, 9, 42179–42191

Hydrogels Based on Hybrid Ionically and Covalently Crosslinked Networks. *J. Appl. Polym. Sci.* **2013**, *130*, 2504−2513.
(3) Gong, J. P. Why are Double Network Hydrogels So Tough? *Soft Matter* **2010**, *6*, 2583−2590.
(4) Myung, D.; Waters, D.; Wiseman, M.; Duhamel, P.-E.; Noolandi, J.; Ta, C. N.; Frank, C. W. Progress in the Development of Interpenetrating Polymer Network Hydrogels. *Polym. Adv. Technol.* **2008**, *19*, 647−657.
(5) Liao, I.-C.; Moutos, F. T.; Estes, B. T.; Zhao, X.; Guilak, F. Composite Three-Dimensional Woven Scaffolds with Interpenetrating Network Hydrogels to Create Functional Synthetic Articular Cartilage. *Adv. Funct. Mater.* **2013**, *23*, 5833−5839.
(6) Çetin, D.; Kahraman, A. S.; Gümüşderelioğlu, M. Novel Scaffolds Based on Poly(2-Hydroxyethyl Methacrylate) Superporous Hydrogels for Bone Tissue Engineering. *J. Biomater. Sci., Polym. Ed.* **2011**, *22*, 1157−1178.
(7) Zeng, M.; Fang, Z. Preparation of Sub-Micrometer Porous Membrane from Chitosan/Polyethylene Glycol Semi-IPN. *J. Membr. Sci.* **2004**, *245*, 95−102.
(8) Zhang, Y.; Liu, J.; Huang, L.; Wang, Z.; Wang, L. Design and Performance of a Sericin-Alginate Interpenetrating Network Hydrogel for Cell and Drug Delivery. *Sci. Rep.* **2015**, *5*, 12374.
(9) Bae, Y. H.; Okano, T.; Ebert, C.; Heiber, S.; Dave, S.; Kim, S. W. Heterogeneous Interpenetrating Polymer Networks for Drug Delivery. *J. Controlled Release* **1991**, *16*, 189−196.
(10) Suthar, B.; Xiao, H. X.; Klempner, D.; Frisch, K. C. A Review of Kinetic Studies on the Formation of Interpenetrating Polymer Networks. *Polym. Adv. Technol.* **1996**, *7*, 221−233.
(11) Yamamoto, N.; Kurisawa, M.; Yui, N. Double-Stimuli-Responsive Degradable Hydrogels: Interpenetrating Polymer Networks Consisting of Gelatin and Dextran With Different Phase Separation. *Macromol. Rapid Commun.* **1996**, *17*, 313−318.
(12) Lohani, A.; Singh, G.; Bhattacharya, S. S.; Verma, A. Interpenetrating Polymer Networks as Innovative Drug Delivery Systems. *J. Drug Delivery* **2014**, *2014*, 583612.
(13) Kong, X.; Narine, S. S. Physical Properties of Sequential Interpenetrating Polymer Networks Produced from Canola Oil-Based Polyurethane and Poly(Methyl Methacrylate). *Biomacromolecules* **2008**, *9*, 1424−1433.
(14) Sperling, L. H. Interpenetrating Polymer Networks: an Overview. *Interpenetrating Polymer Networks*; Advances in Chemistry Series; American Chemical Society, 1994; Vol. *239*, pp 3−38.
(15) Huelck, V.; Thomas, D. A.; Sperling, L. H. Interpenetrating Polymer Networks of Poly(Ethyl Acrylate) and Poly(Styrene-co-Methly Methacrylate). I. Morphology via Electron Microscopy. *Macromolecules* **1972**, *5*, 340−347.
(16) Turner, J. S.; Cheng, Y.-L. Morphology of PDMS−PMAA IPN membranes. *Macromolecules* **2003**, *36*, 1962−1966.
(17) Burford, R. P.; Markotsis, M. G.; Knott, R. B. Real-time SANS Study of Interpenetrating Polymer Network (IPN) formation. *Phys. B* **2006**, *385*, 766−769.
(18) Tominaga, T.; Tirumala, V. R.; Lee, S.; Lin, E. K.; Gong, J. P.; Wu, W.-L. Thermodynamic Interactions in Double-Network Hydrogels. *J. Phys. Chem. B* **2008**, *112*, 3903−3909.
(19) Tominaga, T.; Tirumala, V. R.; Lin, E. K.; Gong, J. P.; Furukawa, H.; Osada, Y.; Wu, W.-L. The Molecular Origin of Enhanced Toughness in Double-Network Hydrogels: A Neutron Scattering Study. *Polymer* **2007**, *48*, 7449−7454.
(20) Endo, H.; Miyazaki, S.; Haraguchi, K.; Shibayama, M. Structure of Nanocomposite Hydrogel Investigated by Means of Contrast Variation Small-Angle Neutron Scattering. *Macromolecules* **2008**, *41*, 5406−5411.
(21) Helminger, M.; Wu, B.; Kollmann, T.; Benke, D.; Schwahn, D.; Pipich, V.; Faivre, D.; Zahn, D.; Cölfen, H. Synthesis and Characterization of Gelatin-Based Magnetic Hydrogels. *Adv. Funct. Mater.* **2014**, *24*, 3187−3196.
(22) Waters, D. J.; Engberg, K.; Parke-Houben, R.; Ta, C. N.; Jackson, A. J.; Toney, M. F.; Frank, C. W. Structure and Mechanism of Strength Enhancement in Interpenetrating Polymer Network Hydrogels. *Macromolecules* **2011**, *44*, 5776−5787.
(23) Leung, B. O.; Chou, K. C. Review of Super-Resolution Fluorescence Microscopy for Biology. *Appl. Spectrosc.* **2011**, *65*, 967−980.
(24) van de Linde, S.; Heilemann, M.; Sauer, M. Live-Cell Super-Resolution Imaging with Synthetic Fluorophores. *Annu. Rev. Phys. Chem.* **2012**, *63*, 519−540.
(25) Moerner, W. E. Microscopy Beyond the Diffraction Limit Using Actively Controlled Single Molecules. *J. Microsc.* **2012**, *246*, 213−220.
(26) Klein, T.; Löschberger, A.; Proppert, S.; Wolter, S.; van de Linde, S. V.; Sauer, M. Live-cell dSTORM with SNAP-tag Fusion Proteins. *Nat. Methods* **2011**, *8*, 7−9.
(27) Wilmes, S.; Staufenbiel, M.; Liße, D.; Richter, C. P.; Beutel, O.; Busch, K. B.; Hess, S. T.; Piehler, J. Triple-Color Super-Resolution Imaging of Live Cells: Resolving Submicroscopic Receptor Organization in the Plasma Membrane. *Angew. Chem., Int. Ed.* **2012**, *51*, 4868−4871.
(28) Muranyi, W.; Malkusch, S.; Müller, B.; Heilemann, M.; Kräusslich, H. G. Super-Resolution Microscopy Reveals Specific Recruitment of HIV-1 Envelope Proteins to Viral Assembly Sites Dependent on the Envelope C-Terminal Tail. *PLoS Pathog.* **2013**, *9*, No. e1003198.
(29) Endesfelder, U.; van de Linde, S.; Wolter, S.; Sauer, M.; Heilemann, M. Subdiffraction-Resolution Fluorescence Microscopy of Myosin-Actin Motility. *ChemPhysChem* **2010**, *11*, 836−840.
(30) Gilbert, T.; Smeets, N. M. B.; Hoare, T. Injectable Interpenetrating Network Hydrogels via Kinetically Orthogonal Reactive Mixing of Functionalized Polymeric Precursors. *ACS Macro Lett.* **2015**, *4*, 1104−1109.
(31) Park, J. W.; Kim, Y.; Lee, K.-J.; Kim, D. J. Novel Cyanine Dyes with Vinylsulfone Group for Labeling Biomolecules. *Bioconjugate Chem.* **2012**, *23*, 350−362.
(32) Sheikholeslami, P.; Muirhead, B.; Baek, D. S. H.; Wang, H.; Zhao, X.; Sivakumaran, D.; Boyd, S.; Sheardown, H.; Hoare, T. Hydrophobically-Modified Poly(Vinyl Pyrrolidone) as a Physically-Associative, Shear-Responsive Ophthalmic Hydrogel. *Exp. Eye Res.* **2015**, *137*, 18−31.
(33) Azuah, R. T.; Kneller, L. R.; Qiu, Y.; Tregenna-Piggott, P. L. W.; Brown, C. M.; Copley, J. R. D.; Dimeo, R. M. DAVE: A Comprehensive Software Suite for the Reduction, Visualization, and Analysis of Low Energy Neutron Spectroscopic Data. *J. Res. Natl. Inst. Stand. Technol.* **2009**, *114*, 341−358.
(34) Kline, S. R. Reduction and Analysis of SANS and USANS Data Using IGOR Pro. *J. Appl. Crystallogr.* **2006**, *39*, 895−900.
(35) Hammouda, B.; Ho, D. L.; Kline, S. Insight Into Clustering in Poly(Ethylene Oxide) Solutions. *Macromolecules* **2004**, *37*, 6932−6937.
(36) Hammouda, B. Scattering from Fractal Systems. In *Probing Nanoscale Structures—The SANS Toolbox*; National Institute of Standards and Technology: Gaithersburg, Marlyand, 2004.
(37) Hammouda, B.; Ho, D. L. Insight into Chain Dimensions in PEO/Water Solutions. *J. Polym. Sci., Part B: Polym. Phys.* **2007**, *45*, 2196−2200.
(38) Shibayama, M.; Isono, K.; Okabe, S.; Karino, T.; Nagao, M. SANS Study on Pressure-Induced Phase Separation of Poly(N-isopropylacrylamide) Aqueous Solutions and Gels. *Macromolecules* **2004**, *37*, 2909−2918.
(39) Ovesný, M.; Křížek, P.; Borkovec, J.; Švindrych, Z.; Hagen, G. M. ThunderSTORM: a Comprehensive ImageJ Plug-in for PALM and STORM Data Analysis and Super-Resolution Imaging. *Bioinformatics* **2014**, *30*, 2389−2390.
(40) Smeets, N. M. B.; Patenaude, M.; Kinio, D.; Yavitt, F. M.; Bakaic, E.; Yang, F.-C.; Rheinstädter, M.; Hoare, T. Injectable Hydrogels with in situ-Forming Hydrophobic Domains: Oligo(D,L-Lactide) Modified Poly(Oligoethylene Glycol Methacrylate) Hydrogels. *Polym. Chem.* **2014**, *5*, 6811−6823.
(41) Geissler, E.; Horkay, F.; Hecht, A.-M. Scattering from Network Polydispersity in Polymer Gels. *Phys. Rev. Lett.* **1993**, *71*, 645−648.

DOI: 10.1021/acsami.7b11637
ACS Appl. Mater. Interfaces 2017, 9, 42179−42191

(42) Shibayama, M.; Tanaka, T.; Han, C. C. Small-Angle Neutron Scattering Study on Weakly Charged Temperature Sensitive Polymer Gels. *J. Chem. Phys.* **1992**, *97*, 6842−6854.
(43) Shibayama, M.; Tanaka, T.; Han, C. C. Small Angle Neutron Scattering Study on Poly(N-Isopropyl Acrylamide) Gels near Their Volume-Phase Transition Temperature. *J. Chem. Phys.* **1992**, *97*, 6829−6841.

DOI: 10.1021/acsami.7b11637
ACS Appl. Mater. Interfaces 2017, 9, 42179−42191